Motion artifact suppression in full-field optical coherence tomography

Delphine Sacchet, Michal Brzezinski, Julien Moreau, Arnaud Dubois

Motion artifact suppression in full-field optical coherence tomography

Delphine Sacchet,* Michal Brzezinski, Julien Moreau,
Patrick Georges, and Arnaud Dubois

Laboratoire Charles Fabry de l'Institut d'Optique, CNRS UMR 8501, Université Paris-Sud,
Campus Polytechnique, RD128, 91127 Palaiseau Cedex, France

*Corresponding author: delphine.sacchet@institutoptique.fr

Significant motion artifacts limit the performance of conventional full-field optical coherence tomography (FF-OCT) for *in vivo* imaging. We present a theoretical and experimental study of those limitations. A new FF-OCT system suppressing most of artifacts due to sample motions is demonstrated using instantaneous phase shifting with nonpolarizing optics and pulsed illumination. The experimental setup is based on a Linnik-type interferometer illuminated by the superluminescence emission from a $Ti:Al_2O_3$ waveguide crystal. En face tomographic images are calculated as a combination of two phase-opposed interferometric images acquired simultaneously by two CCD cameras placed at both outputs of the interferometer, with a spatial resolution of $0.8\,\mu$m $\times$ $1.6\,\mu$m (axial × transverse) and a detection sensitivity of $\sim$60 dB.   © 2010 Optical Society of America

OCIS codes: 170.4500, 170.3880, 180.3170.

1. Introduction

In recent years, the possibility of using light for biological tissue imaging has received much attention. By revealing optical contrasts, such as absorption, scattering, reflection, or birefringence, optical imaging provides additional information to those given by nonoptical imaging methods, such as ultrasounds, x rays, and magnetic resonance. Optical coherence tomography (OCT) rapidly turned out to be the optical technique of choice for noninvasive high-resolution imaging of biological media [1,2].

OCT performs optical sectioning in the sample, making three-dimensional (3D) reconstruction of internal structures possible. Sectional images can be categorized into two types: longitudinal images parallel to the optical axis and transverse (en face) images perpendicular to the optical axis. En face imaging is of particular interest in applications where the transverse distribution of biological structures has to be examined and may complement information provided by the longitudinal images [3,4].

Two distinct methods have been successively developed for obtaining longitudinal sectional images: time-domain OCT (TD-OCT), wherein the images are acquired point by point by scanning both the interferometer reference arm length and the laser beam in the transverse direction [1], and Fourier-domain OCT (FD-OCT), where the reference arm length scan is replaced by spectroscopic measurements [5,6]. In TD-OCT, the time required to acquire the interferometric signal at each point can be extremely short (1–$10\,\mu$s) [7,8]. However, in the case of high axial resolution, a long acquisition time is required with TD-OCT to achieve sufficient detection sensitivity, since axial resolution and sensitivity are inversely proportional [9]. Moreover, because of the time delay between the acquisition of distant points, motion artifacts can appear in *in vivo* imaging. In the FD-OCT technique, the removal of axial scanning reduces the image acquisition time by a factor of $\sim$100 [10]. Motion artifacts are then imperceptible for most applications, making *in vivo* imaging very common [11].

For obtaining en face OCT images, two distinct techniques have been proposed: en face TD-OCT using two-dimensional (2D) beam scanning and a single detector [3], and full-field OCT (FF-OCT) based on low-coherence interference microscopy [12,13]. In FF-OCT, the image acquisition relies on the use of an array camera. 3D imaging is achieved by scanning the object in the axial direction. The interferometric information is conventionally extracted by a phase-shifting method: several interferometric images (frames) are acquired, a phase shift being introduced between successive frames by using, for example, a photoelastic phase modulator [14] or by displacing the reference mirror [12]. Then, the amplitude of the interference signal, i.e., the fringe envelope, is calculated by combination of these frames. A number of phase-shifting methods have been proposed, using 2, 4, or 7 frames with steps or sinusoidal phase modulations [14–18]. Nevertheless, these phase-shifting methods are not suitable for imaging moving objects, for two main reasons. First, the object motion may create a change in the phase of the interferometric signal during the acquisition of each frame, which leads to a reduction of the tomographic image contrast due to the blurring of the interference. This problem can be solved by reducing the acquisition time or the exposure time of each frame, provided that a sufficiently intense light source is used [4,19]. Another problem arises from the fact that the frames are acquired sequentially in time. Because of sample motion, the intensity of light received by some pixels of the camera may change between successive frames, which creates an intrusive signal in the calculated tomographic image. To solve this problem, several types of instantaneous phase-shifting methods have been proposed. All these techniques use polarization optics to produce at least two phase-stepped images, which are acquired simultaneously with one or several camera(s) [19–21]. The drawback with these polarization-sensitive techniques is that artifacts may occur when imaging birefringent media, such as cornea or muscles [4]. Moreover, these methods usually imply the use of broadband wave plates, whose performance is limited. By exploiting the inherent phase shifts of fiber-optic couplers and conservation of energy, unpolarized instantaneous phase shifting has been implemented in both TD-OCT and FD-OCT [22], but has not been demonstrated in FF-OCT so far, to our knowledge.

In this paper, we study, theoretically and experimentally, motion artifacts in FF-OCT. To suppress these artifacts, we have developed an original instantaneous phase-shifting FF-OCT setup based on nonpolarizing optics. This ultrahigh-resolution imaging system operates in the 800 nm wavelength region, by use of a new low-coherence illumination source, based on the pulsed amplified spontaneous emission from a titanium-doped sapphire ($Ti:Al_2O_3$) waveguide and two identical cameras to acquire simultaneously two phase-opposed images. We present the FF-OCT setup and its performance in terms of power, stability, spatial resolution, and detection sensitivity. Motion artifacts suppression is demonstrated using this setup, and a 3D image of a human nail fold, *in vivo*, is presented.

2. Motion Artifacts in Conventional FF-OCT

Studying and reducing image artifacts resulting from motion has received much attention in nearly all biomedical imaging modalities because these artifacts degrade image quality and even cause inaccurate clinical interpretation [23–25]. FF-OCT has been widely reported as a powerful technique for *in vitro* high-resolution imaging. However, conventional FF-OCT is not appropriate for *in vivo* applications because motion artifacts severely degrade the imaging performance. Only a few studies have been conducted on the causes and limitations of these artifacts. Moreover, few solutions have been proposed to properly overcome these limitations [19–21]. In this section, we propose a theoretical and experimental study of motion artifacts in conventional FF-OCT. We distinguish the effect of both axial motion (i.e., along the microscope objectives axis) and transverse motion (i.e., perpendicular to the microscope objective axis). The experimental study was carried out with a conventional FF-OCT setup using sinusoidal phase shifting to acquire two phase-opposed frames. With this setup, the spatial resolution is $1.4\,\mu m \times 1.6\,\mu m$ (axial × transverse). The detector used for the detection is a silicon-based CCD camera (Model CA-D1 from Dalsa, 256×256 pixels, 8 bits, 200 Hz) with an integration time of 5 ms, a pixel size of $16\,\mu m$, and a full-well capacity of 1.2×10^5 electrons.

A. Emergence of an Intrusive Signal because of Transverse Motion

In conventional FF-OCT, several frames are acquired sequentially in time and the tomographic image is calculated by combination of these different frames. The tomographic signal is generated by the variation of the interferometric signal induced by the applied phase shift between these successive frames. However, the intensity received by each pixel may also vary because of the sample motion, which changes the position of biological structures in successive frames. This variation of intensity generates an intrusive signal, which superimposes to the tomographic signal. In the case of FF-OCT with relatively low NA, this intrusive signal results essentially from transverse motion of internal structures inside and/or outside the coherence volume. Axial motion has much less influence on the intrusive signal, since it only causes a defocusing, which does not change significantly the intensity of light received by each pixel. This intrusive signal causes a misinterpretation of the tomographic images. The sectioning ability of the imaging system may also be degraded if scattering structures outside the coherence volume move. This effect was illustrated by imaging a region ($200\,\mu m \times 200\,\mu m$) of a microscope calibration star

target, composed of chrome bands deposited on a glass substrate (contrast of ~0.94). By using a piezo-electric stage actuator, the target was animated by a transverse motion with constant speed of ~2 mm/s and a direction roughly orthogonal to the stripped pattern (see Fig. 1(b)). The value of the speed was adjustable from 0 to 5 mm/s and was intentionally chosen high to enhance the intrusive signal. A tomographic image, obtained during this transverse displacement with conventional FF-OCT, is shown in Fig. 1(b). The target was placed ~10 μm away from the coherence plane to isolate the effect of the intrusive signal. In principle, no signal should appear in the tomographic image because the reflecting structures are located outside the coherence volume. In practice, an important intrusive signal was observed in the regions near the edges of the stripes, where the intensity of the interferometric signal has varied between both frames due to the transverse motion.

We propose a model for evaluating the maximal transverse speed of the sample that can be tolerated in conventional FF-OCT. We consider an acquired image presenting an intensity profile along a line of the CCD camera described in Fig. 2. In the model presented below, this intensity is converted into an equivalent reflectivity R. The intensity profile can result from sample reflectivity variations, and also from interference (including speckle).

The signal delivered by a pixel of surface p^2 imaging an area of the sample of surface $(p/\gamma)^2$, where γ is the magnification of the optical system, and with a reflectivity $R_{\max}$ (see Fig. 2(a)) is

$$S_1 = k \left(\frac{p}{\gamma} \right)^2 R_{\max}, \qquad (1)$$

where k is a proportionality coefficient, which mainly depends on the quantum efficiency and the integration time of the CCD camera.

After transverse displacement of the sample by a distance x (see Fig. 2(b)), the signal delivered by the same pixel, equal to the integral of the reflectivity profile along the transverse direction, becomes

$$S_2 = S_1 - k \frac{p}{\gamma} \frac{R_{\max} - R_{\min}}{2\Delta x} x^2. \qquad (2)$$

The variation of the signal due to the transverse motion can be detected if it is superior to the noise. We consider that the smallest variation, induced by a minimal transverse displacement $x_{\min}$, is the noise value. Assuming that the camera is operating close to saturation, the signal is proportional to the full-well capacity ξ_{sat}, whereas the noise is proportional to its square root. Therefore, the signal-to-noise-ratio (SNR) is

$$\mathrm{SNR} = \frac{S_1}{(S_1 - S_2)_{\min}} = \sqrt{\xi_{sat}}, \qquad (3)$$

$$x_{\min} = \sqrt{\frac{2\Delta x p}{\gamma \sqrt{\xi_{\mathrm{sat}}}} \times \frac{R_{\max}}{R_{\max} - R_{\min}}}, \qquad (4)$$

The parameter Δx is related to the reflectivity profile of the sample, but cannot be inferior to the transverse resolution of the imaging system. If we consider this parameter equal to the transverse resolution $\Delta x = 1.6 \,\mu m$, a pixel size $p = 16 \,\mu m$, a magnification $\gamma = 17$, and a full-well capacity $\xi_{\mathrm{sat}} = 10^5$, the minimal transverse displacement is $x_{\min} = 0.1 \,\mu m$. In the case of a continuous displacement of the sample, Eq. (4) is not strictly valid, but it may give an order of magnitude for the maximal transverse speed of the sample. Considering an integration time of the camera $T_{\mathrm{int}} = 5 \,ms$, the maximal transverse speed is $v_{\max} \sim 20 \,\mu m/s$.

The previous calculation was done for a sequential transverse displacement and a sample with a contrast of 1 (i.e., $R_{\max} = 1$ and $R_{\min} = 0$). We performed numerical calculations to take into account the continuous transverse displacement of the sample during the integration time of the camera. The maximal transverse speed obtained with numerical calculations as a function of the sample contrast is shown in Fig. 3. The contrast was calculated with a maximal reflectivity $R_{\max} = 1$ (because the incident optical power is adjusted in function of the maximal reflectivity of the sample so that the camera always works close to saturation) and an adjustable minimal reflectivity $R_{\min}$. As expected, the constraint on the
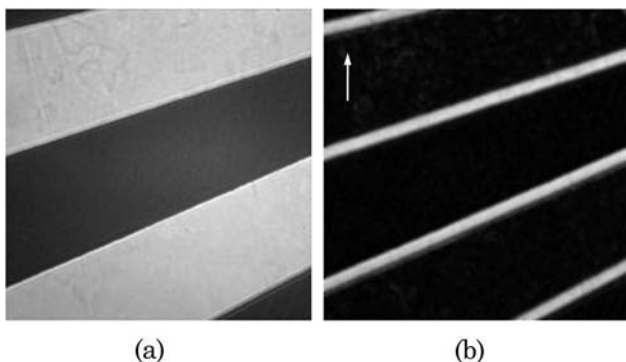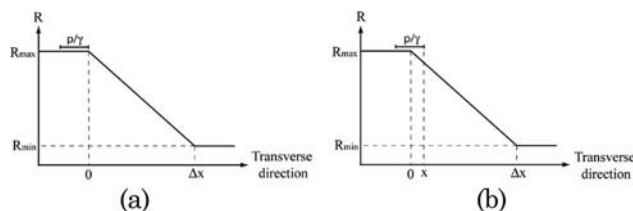

Fig. 1. (a) Conventional image of a microscope calibration star target. (b) Conventional FF-OCT image of the target placed outside the coherence volume and animated by a transverse motion in a direction indicated by the arrow (right). Image size: 200 μm × 200 μm.

Fig. 2. Equivalent reflectivity profile used in our model for evaluating the maximal transverse speed. $R_{\max}$ and $R_{\min}$ are the maximum and minimum reflectivity of the sample, and p/γ is the width of a camera pixel in the sample plane, where γ is the magnification of the optical system.
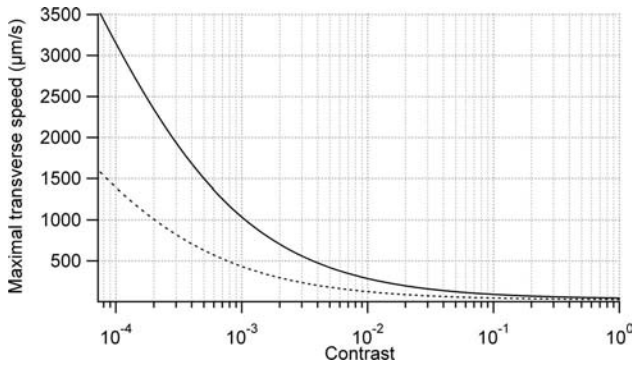
Fig. 3. Maximal transverse speed versus contrast of the sample. The numerical calculations for a linear transverse displacement of the sample are represented by the solid curve and computation of Eq. (4) by the dotted curve.
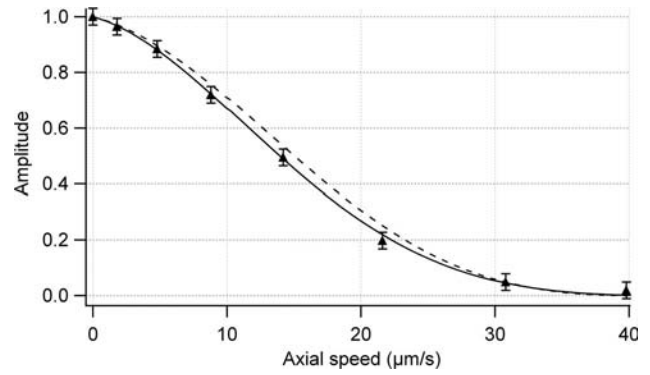

Fig. 4. Amplitude of the tomographic signal versus axial speed of the object for continuous illumination and successive phase shifting. The numerical calculations for sinusoidal phase shifting and polychromatic illumination are represented by the solid curve, computation of Eq. (5) by the dotted curve, and the measurements by the triangles.

tolerable transverse speed is not so severe because the variation of intensity due to transverse movement is averaged during the integration time. For example, the maximal tolerable transverse speed for a sample with a contrast of 10^{-4} (i.e., $R_{max} = 1$ and $R_{min} = 0.9998$) is $\sim 3.5 \, \mathrm{mm/s}$. This contrast results from any effect that induces spatial intensity variations, such as reflection inhomogeneities within the sample and interference (including speckle).

B. Fringe Blurring from Axial Motion

The object motion creates a variation of both the phase and the amplitude of light received by the camera pixels. The variation of the phase during the integration time of each frame causes a blurring of the interference, which leads to a loss of the tomographic signal. This effect is mainly due to a motion in the axial direction. The problem can be overcome by reducing the illumination time or the acquisition time of each frame.

We have theoretically studied the effect of fringe blurring in conventional FF-OCT using two phase-opposed frames acquired successively. Assuming monochromatic illumination and step phase shifting, the tomographic image, calculated as the square difference of the two frames (S_1, S_2), is

$$(S_1 - S_2)^2 \propto \mathrm{sinc}^2\left(\frac{4\pi}{\lambda_0} v T_{\mathrm{int}}\right), \tag{5}$$

where λ_0 is the wavelength of the illumination source, v is the axial speed of the object, and T_{int} is the integration time of each frame. The tomographic signal drops to zero for a speed v_{max}, which can be regarded as the maximal tolerable speed:

$$v_{max} = \frac{\lambda_0}{4 T_{\mathrm{int}}}. \tag{6}$$

For an integration time of the camera $T_{\mathrm{int}} = 5 \, \mathrm{ms}$ and an illumination source spectrum centered at $\lambda_0 = 800 \, \mathrm{nm}$, the maximal axial speed is equal to $v_{max} \sim 40 \, \mu \mathrm{m/s}$, which is within the typical range of biological tissue movements. The maximal tolerable speed found with numerical calculations, taking

into account polychromatic illumination and sinusoidal phase shifting, is similar (see Fig. 4).

We also performed measurements of the amplitude of the tomographic signal as a function of the axial speed of the object. This experiment was done with continuous illumination and an integration time by the camera of 5 ms. The object is a mirror mounted on a piezoelectric stage actuator, which applies a strict axial motion. The axial position of the mirror at zero voltage applied to the piezoelectric coincided with the focal plane of the microscope objective. Figure 4 shows both the numerical calculations and the measurements of the decrease of the amplitude of the tomographic signal as a function of axial speed, which are in good agreement.

In conclusion, the range of typical biological tissue movement speeds corresponds to the maximal tolerable axial speed for which the interferometric signal is completely blurred. This is a severe limitation of conventional FF-OCT for *in vivo* imaging. Therefore, a shorter integration time is absolutely required to overcome this limitation.

3. Instantaneous Phase-Shifting FF-OCT with Pulsed Illumination

The previous theoretical study has shown how several key experimental parameters play a crucial role in motion artifact limitations. Guided by this study, we have developed an original system, which is presented in this section. The system uses a novel pulsed illumination source to reduce the exposure time and instantaneous phase shifting with nonpolarizing optics to suppress the intrusive signal.

A. Fluorescence-Based Illumination Source

To perform *in vivo* imaging, a short illumination time or a short integration time by the camera is necessary. The use of high-speed cameras is not suitable because of their small dynamic range, which limits the detection sensitivity [4]. A better solution consists of combining a camera with high full-well capacity and a pulsed illumination source to reduce the
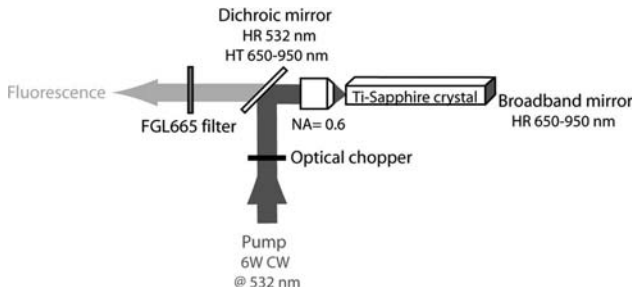
Fig. 5. Schematic representation of the superluminescent Ti:Al$_2$O$_3$ light source. A contrapropagating configuration is used to collect the fluorescence. HR, high reflectivity; HT, high transmission; NA, numerical aperture.

Fig. 6. Output fluorescent power sent into the FF-OCT setup versus incident pump power.

exposure time. Light pulses can be produced with a halogen lamp by using an optical chopper. However, the available optical power is then too low to cover the entire dynamic range of the detector when imaging biological samples. To overcome this problem, we have developed a new illumination source based on the broadband fluorescence of a Ti:Al$_2$O$_3$ waveguide crystal, which can provide much higher brightness in the useful wavelength range.

The principle of our superluminescent source is shown schematically in Fig. 5. A frequency-doubled neodymium vanadate (Nd:YVO$_4$) laser pumps a Ti:Al$_2$O$_3$ square-shaped waveguide crystal (1.24 mm ×1.24 mm × 10 mm) with 0.1 wt. % Ti$_2$O$_3$ in Al$_2$O$_3$. With a linear polarized pump laser, the absorption cross section for the $^2T_2 \rightarrow \ ^2E$ transition in Ti:Al$_2$O$_3$ is around 6.5×10^{-20} cm^2. The fluorescence lifetime of this transition is around $3.15\,\mu$s at room temperature [26]. These small dimensions of the crystal and the guiding of the emitted fluorescence by total internal reflection maximize the collection efficiency and so the output power. The pump laser can be pulsed by an optical chopper with a repetition rate of 200 Hz and pulse duration adjustable from $500\,\mu$s to 2 ms. Because of the absorption of the pump laser along the crystal, the fluorescent power is higher at the beginning of the crystal. To maximize the collection efficiency, a contrapropagating configuration was developed. In this configuration, the pump light passes through a dichroic mirror that reflects more than 99% of the pump light at 532 nm and transmits ~90% of the fluorescence (650–950 nm). The pump beam is focused inside the crystal by a microscope objective ($f = 15$ mm, 0.6 NA, and 4.1 mm working distance). Single-pass geometry is enough to absorb more than 80% of the pump power. The fluorescence emitted in the copropagating direction is retroreflected by a broadband mirror, and the fluorescence emitted in the contrapropagating direction is collected and collimated by the same microscope objective, which sets the divergence of the output beam. A long-pass colored glass filter (FGL665) after the dichroic mirror removes any residual pump.

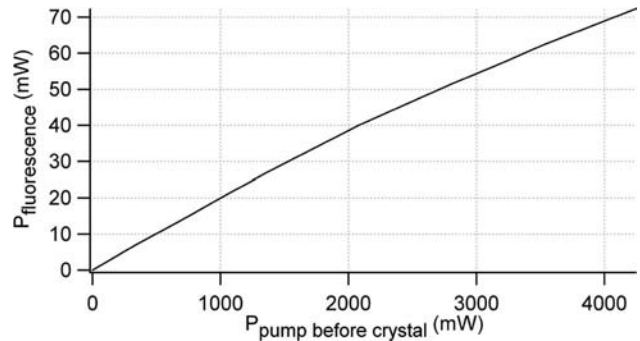Figure 6 shows the CW *fluorescence power* sent into the FF-OCT setup versus the incident pump power. Cooling of the crystal at 18 °C was applied to remove any saturation effect due to thermal effects. For an incident power of 4.2 W, a fluorescence power of 72 mW was achieved, which corresponds to a conversion efficiency of 2%. The fluorescence power is here limited by the available pump power and could be easily increased. By using a pump laser emitting a 1 ms pulse at a repetition rate of 200 Hz, a millisecond pulse regime is easily achievable with an energy per pulse of $72\,\mu$J. According to our theoretical study, this pulse duration is short enough to make the fringe blurring effect insignificant. The fluorescence of a bulk Ti:Al$_2$O$_3$ crystal as a CW illumination source has already been implemented in conventional TD-OCT with a brightness 2 orders of magnitude higher than ours [27]. However, such brightness is not necessary in FF-OCT because our superluminescent source emits enough light to saturate the array camera even in the pulsed regime. The crucial parameter here is to have a wide-field illumination with a good spatial homogeneity. With the total internal reflection guiding, the spatial profile of the fluorescence beam is somewhat modulated because of the spatial mode of the square-shaped waveguide. To suppress this spatial inhomogeneity, the fluorescence beam was spatially filtered. In this configuration, the homogeneity over the whole microscope objective fields was similar to the one obtained with the halogen lamp incorporated in a Köhler illuminator.

B. Unpolarized Instantaneous Phase-Shifting FF-OCT

The experimental setup of our unpolarized instantaneous phase-shifting FF-OCT system is represented schematically in Fig. 7. The setup is based on a Linnik interferometer, corresponding to a Michelson interferometer with identical microscope objectives in both arms (water immersion, 10×, 0.3 NA, and 3 mm working distance, from Olympus) [14,28]. Light emitted by the superluminescent source is split into both arms by a nonpolarizing 50–50 broadband beam splitter. A polished surface of YAG (Y$_3$Al$_5$O$_{12}$) crystal, providing a reflectivity of 2.5% in water, is placed in the reference arm of the Linnik interferometer in the focal plane of the microscope objective. Both outputs of the interferometer are acquired
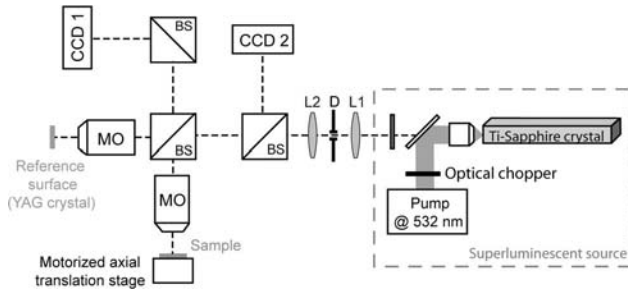
Fig. 7. Schematic representation of the unpolarized instantaneous phase-shifting FF-OCT setup. BS, nonpolarizing broadband beam splitters; MO, microscope objectives; L1, L2, lenses; D, diaphragm; superluminescent source as described in Fig. 4.

simultaneously by two synchronized identical silicon-based CCD cameras (Model CA-D1 from Dalsa, 256×256 pixels, 8 bits, 200 Hz, maximum sensitivity around 800 nm). A second broadband nonpolarizing 50–50 beamsplitter is placed before the Linnik interferometer to separate the interferometric signal from the illumination input. 3D imaging is obtained by axial scanning of the sample using a motorized axial translation stage. To equalize roughly the optical intensity received by each camera, a third broadband nonpolarizing 50–50 beam splitter is placed at the second output of the interferometer. Compared to conventional FF-OCT, the introduction of two additional beam splitters reduces the illumination fluence on the sample by 50% and on the cameras by 75%. Nevertheless, the available fluence delivered by the fluorescence source was high enough to compensate these losses, since the effective energy per pulse incident on the sample was $\sim 2\,\mu J$, leading to a fluence of $\sim 6\,\mu J/cm^2$. To simplify the alignment procedure, no lens was used to project the interferometric images onto the cameras. The microscope objectives are, therefore, not used at an infinite conjugate ratio, for which they are optimized. However, very few optical aberrations are observed and they are identical for both cameras. With this conjugation, the effective NA of the microscope objectives is slightly decreased, but no significant consequence on transverse resolution degradation was observed. In this configuration, we measured a transverse magnification of 20 between the sample and the camera.

The principle of unpolarized instantaneous phase-shifting FF-OCT is based on energy conservation. The signal delivered by each pixel of CCD 1 can be expressed as

$$S_1(x,y) \propto \frac{I_0}{4}\left[R_{ref} + R_{inc} + R_{coh}(x,y) \right.$$
$$\left. + 2\sqrt{R_{ref}R_{coh}(x,y)}\cos(\varphi(x,y))\right], \quad (7)$$

where I_0 represents the intensity of the illumination source, R_{ref} is the reflectivity of the reference surface, R_{inc} is the proportion of incoherent light, resulting essentially from backscattering and backreflection by structures within the object localized outside

the coherence volume, R_{coh} is the proportion of coherent light backscattered by structures within the object localized inside the coherence volume, and φ is the optical phase.

Because of the conservation of energy, the signal delivered by each pixel of CCD 2 is

$$S_2(x,y) \propto \frac{I_0}{4}\left[R_{ref} + R_{inc} + R_{coh}(x,y) \right.$$
$$\left. - 2\sqrt{R_{ref}R_{coh}(x,y)}\cos(\varphi(x,y))\right]. \quad (8)$$

The interferometric images acquired by both cameras are thus in phase opposition and the tomographic image is calculated from the squared difference of these two images:

$$(S_1 - S_2)^2 \propto R_{coh}\cos^2\varphi. \quad (9)$$

Actually, the fringe envelope R_{coh} is not truly extracted because the phase φ is not eliminated. A phase-shifting method using a combination of more than two interferometric images is required to eliminate it. However, due to the size and distribution of the structures in most biological samples, interference fringes are generally not visible in the images.

In our method, the two phase-opposed interferometric images are acquired simultaneously by two different detectors, and their squared difference leads to the tomographic image. Combining these two interferometric images requires precise positioning of the cameras and calibration of the CCD pixel responses. A pixel located at the same coordinates on both cameras has to be conjugated with the same area in the sample; otherwise the difference of two identical spatially shifted images would lead to an additional signal in the tomographic image, irrelevant to the sample. To realize a subpixel superposition of both array detectors, the six degrees of freedom have to be adjusted. Two degrees of rotation are set by autocollimation with a He–Ne laser beam. A microscope calibration target is used to adjust the three degrees of translation and the last degree of rotation. Real-time calculation of the correlation between a pair of images of a reflecting surface with random roughness is finally applied to optimize the adjustments. Because this alignment is sample independent, it is performed only once before the experiments. The mean intensities received by both cameras also have to be identical and are normalized by a numerical calibration done *a posteriori*.

The *axial resolution*, which is generally defined as the full width at half-maximum (FWHM) Δz of the interferogram, is determined by the coherence length of the illumination source and is given by

$$\Delta z = \frac{2\ln 2}{n\pi}\left(\frac{\lambda^2}{\Delta\lambda}\right), \quad (10)$$

where n is the refractive index of the medium, λ is the center wavelength, and $\Delta\lambda$ is the effective optical
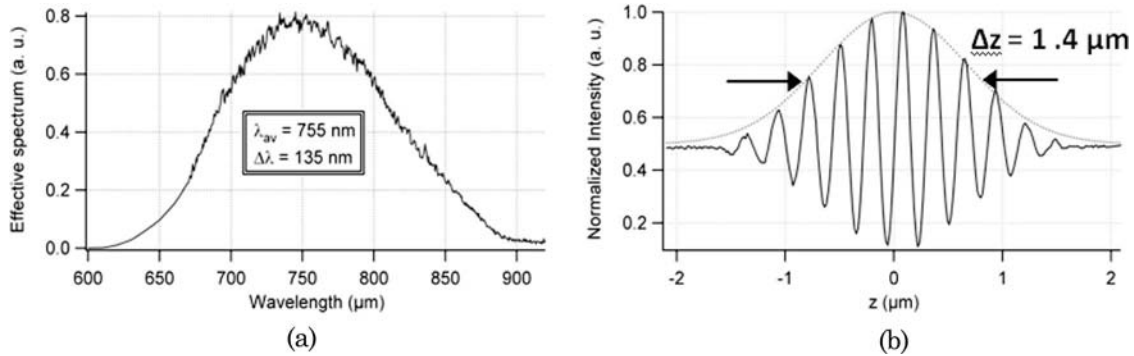
Fig. 8. (a) Effective optical spectrum of the FF-OCT setup, given by the product of the spectrum of the fluorescent source and the spectral response of the camera. The bandwidth is 135 nm centered at 755 nm. (b) Interferogram measured by the FF-OCT setup in water. The axial resolution is 1.4 µm.

spectrum width (FWHM), which is given by the product of the spectrum of the fluorescent source, the spectral transmission of the optical components, and the spectral response of the camera. Figure 8(a) shows the experimental effective optical spectrum, which is the product between the experimental fluorescence spectrum of the $Ti:Al_2O_3$ crystal and the spectral response of the cameras. The FWHM bandwidth was around 135 nm centered at 755 nm. Figure 8(b) shows the corresponding interferogram measured with the FF-OCT setup in water. The FWHM of the fringe envelope was found to be 1.4 µm, which is in good agreement with theoretical calculations from Eq. (10).

The *transverse resolution* was measured by recording an intensity profile across a cleaved mirror. The response is the convolution of a perfect edge and the point spread function (PSF) and a rectangular function (which simulates the image sampling by the camera pixels). With our 0.3 NA microscope objectives, the FWHM of the PSF was found to be 1.4 µm, in accordance with the expected theoretical value using a NA of 0.3.

The *detection sensitivity*, which determines the imaging contrast and penetration depth, was measured to be close to the theoretical sensitivity given by

$$R_{\min} = \frac{(R_{\text{ref}} + R_{\text{inc}})^2}{4N\xi_{\text{sat}}R_{\text{ref}}}, \quad (11)$$

where ξsat represents the full-well capacity of the camera pixels, and N is the number of accumulated images. With our setup, a detection sensitivity of ∼90 dB is achievable with 200 accumulations, as in conventional FF-OCT [13]. However, this number of accumulations is not realistic for *in vivo* applications. Without accumulation, the detection sensitivity was measured to be ∼60 dB. This moderate sensitivity, however, proved sufficient to image biological structures at modest penetration depths in weakly scattering media. The detection sensitivity can be increased without image accumulation by applying pixel binning, consisting of taking square groups of pixels and combining them into "super" pixels, capable of holding much more light. For exam-

ple, operating in 4 × 4 binning mode increases the detection sensitivity by ∼12 dB. However, pixel binning is only suitable with cameras having a large number of pixels, which is not the case with the cameras used here (256 × 256 pixels).

4. Suppression of Motion Artifacts

A. Suppression of the Intrusive Signal from Transverse Motion

In conventional FF-OCT, the apparition of an intrusive signal is mainly due to the fact that several frames are acquired sequentially in time. With our instantaneous phase-shifting method, this signal is suppressed because of the simultaneous acquisition of two phase-opposed images. This effect was highlighted by imaging the microscope calibration target described in Subsection 3.A. This target was mounted on a transverse translation stage and was imaged during its displacement with both the successive and instantaneous phase-shifting methods. The tomographic images shown in Fig. 9 were acquired ∼10 µm away from the coherence plane to study the effect of the intrusive signal only. As expected, the comparison between the successive (Fig. 9(a)) and instantaneous (Fig. 9(b)) phase-shifting methods demonstrates a suppression of the intrusive signal with our motion insensitive FF-OCT setup. This en
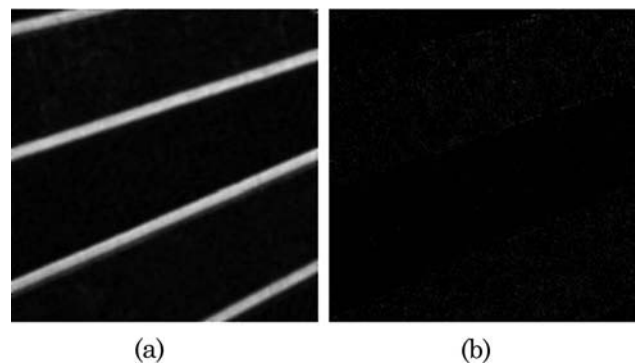

Fig. 9. (a) Tomographic images of a microscope calibration target animated by a transverse motion with successive and (b) instantaneous acquisition of frames. Image size: 200 µm × 200 µm.
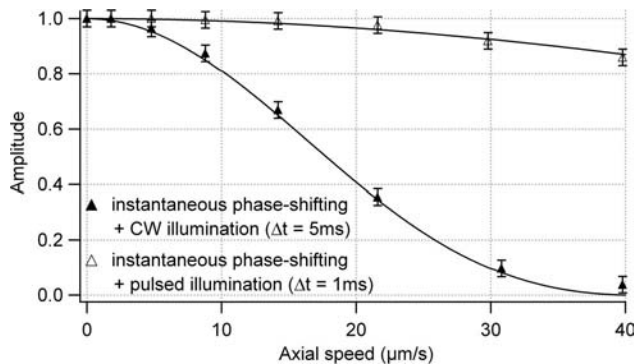
Fig. 10. Amplitude of the tomographic signal as a function of the axial speed of the sample for continuous and pulsed illumination. The numerical simulations are represented by the solid curves and the measurements by the triangles.

face tomographic image was acquired within an acquisition time of 1 ms, which is short enough for 2D *in vivo* imaging.

B. Reduction of Fringe Blurring from Axial Motion

In conventional FF-OCT, the object motion creates a variation of both the phase and the amplitude of the light received by the camera pixels. The variation of the phase during the integration time of each frame causes a blurring of the interference, which leads to a loss of the tomographic signal. We also studied the effect of the reduction of the exposure time on the amplitude of the tomographic signal. It was measured for the instantaneous phase-shifting method with both the continuous regime (with an integration time by the cameras of 5 ms) and the pulsed regime (with an illumination time of 1 ms) as a function of the axial speed by mounting a sample mirror on a piezoelectric stage actuator. The axial position of the sample mirror at zero voltage applied to the piezoelectric coincided with the focal plane of microscope objectives and the axial speed was calibrated as a function of the frequency and voltage applied to the piezoelectric. Figure 10 shows the measurement of the decrease of the amplitude for both illumination regimes, which are in good agreement with numerical simulations. As expected, reducing the illumination time by a factor of 5 tolerates an axial speed 5 times higher.

5. Conclusion

In this paper, we have presented a theoretical and experimental study of motion artifacts in FF-OCT. A new FF-OCT system was designed to suppress those motion artifacts. Intrusive signal, generated essentially by transverse motion of the sample, is suppressed by implementation of an instantaneous phase-shifting method insensitive to polarization. Fringe blurring, induced mainly by axial motion of the sample, is dramatically reduced by using a pulsed illumination source, based on the fluorescence of a Ti : Al$_2$O$_3$ waveguide crystal. A spatial resolution of $0.8\,\mu m \times 1.6\,\mu m$ (axial × transverse) and a detection sensitivity around 60 dB are reported. This mod-

erate detection sensitivity could easily be improved by using cameras with a large number of pixels to perform pixel binning.

References

1. D. Huang, E. A. Swanson, C. P. Lin, J. S. Schuman, W. G. Stinsin, W. Chang, M. R. Hee, T. Flotte, K. Gregory, C. A. Puliafito, and J. G. Fujimoto, "Optical coherence tomography," Science **254**, 1178–1181 (1991).
2. A. F. Fercher, "Optical coherence tomography," J Biomed. Opt. **1**, 157–173 (1996).
3. A. G. Podoleanu, G. M. Dobre, and D. A. Jackson, "En-face coherence imaging using galvanometer scanner modulation," Opt. Lett. **23**, 147–149 (1998).
4. K. Grieve, A. Dubois, M. Simonutti, M. Paques, J. Sahel, J. F. Le Gargasson, and C. Boccara, "*In vivo* anterior segment imaging in the rat eye with high speed white-light full-field optical coherence tomography," Opt. Express **13**, 6286–6295 (2005).
5. A. F. Fercher, C. K. Hitzenberg, G. Kamp, and S. Y. Elzaiat, "Measurement of intraocular distance by backscattering spectral interferometry," Opt. Commun. **117**, 43–48 (1995).
6. R. A. Leitgeb, W. Drexler, A. Unterhuber, B. Hermann, T. Bajraszewski, T. Le, A. Stingl, and A. F. Fercher, "Ultrahigh resolution Fourier domain optical coherence tomography," Opt. Express **12**, 2156–2165 (2004).
7. G. J. Tearney, B. E. Bouma, S. A. Boppart, B. Golubovic, E. A. Swanson, and G. J. Fujimoto, "Rapid acquisition of *in-vivo* biological images by use of optical coherence tomography," Opt. Lett. **21**, 1408–1410 (1996).
8. A. M. Rollins, S. Yazdanfar, M. D. Kulkarni, R. Ung-Arunyawee, and J. A. Izatt, "*In vivo* video rate optical coherence tomography," Opt. Express **3**, 219–229 (1998).
9. E. A. Swanson, D. Huang, M. R. Hee, J. G. Fujimoto, C. P. Lin, and C. A. Puliafito, "High speed optical coherence domain reflectometry," Opt. Lett. **17**, 151–153 (1992).
10. M. Wojtkowski, V. J. Srinivasan, T. H. Ko, J. G. Fujimoto, A. Kowalczyk, and J. S. Duker, "Ultrahigh-resolution, high-speed, Fourier domain optical coherence tomography and methods for dispersion compensation," Opt. Express **12**, 2404–2422 (2004).
11. N. A. Nassif, B. Cense, B. H. Park, M. C. Pierce, S. H. Yun, B. E. Bouma, G. J. Tearney, T. C. Chen, and J. F. de Boer, "*In vivo* high-resolution video-rate spectral-domain optical coherence tomography of the human retina and optic nerve," Opt. Express **12**, 367–376 (2004).
12. L. Vabre, A. Dubois, and A. C. Boccara, "Thermal-light full-field optical coherence tomography," Opt. Lett. **27**, 530–533 (2002).
13. A. Dubois, K. Grieve, G. Moneron, R. Lecaque, L. Vabre, and A. C. Boccara, "Ultrahigh-resolution full-field optical coherence tomography," Appl. Opt. **43**, 2874–2883 (2004).
14. A. Dubois, L. Vabre, A. C. Boccara, and E. Beaurepaire, "High-resolution full-field optical coherence tomography with a Linnik microscope," Appl. Opt. **41**, 805–812 (2002).
15. A. Dubois, G. Moneron, and A. C. Boccara, "Thermal-light full-field optical coherence tomography in the $1.2\,\mu m$ wavelength region," Opt. Commun. **266**, 738–743 (2006).
16. A. Dubois, G. Moneron, K. Grieve, and A. C. Boccara, "Three-dimensional cellular-level imaging using full-field optical coherence tomography," Phys. Med. Biol. **49**, 1227–1234 (2004).
17. B. Laude, A. De Martino, B. Drévillon, L. Benattar, and L. Schwartz, "Full-field optical coherence tomography with thermal light," Appl. Opt. **41**, 6637–6645 (2002).
18. J. Na, W. J. Choi, E. S. Choi, S. Y. Ryu, and B. H. Lee, "Image restoration method based on Hilbert transform for full-field optical coherence tomography," Appl. Opt. **47**, 459–466 (2008).

19. G. Moneron, A. C. Boccara, and A. Dubois, "Stroboscopic ultra-high-resolution full-field optical coherence tomography," Opt. Lett. **30**, 1351–1353 (2005).

20. M. S. Hrebesh, R. Dabu, and M. Sato, "*In vivo* imaging of dynamic biological specimen by real-time single-shot full-field optical coherence tomography," Opt. Commun. **282**, 674–683 (2009).

21. M. Akiba, K. P. Chan, and N. Tanno, "Full-field optical coherence tomography by two-dimensional heterodyne detection with a pair of CCD cameras," Opt. Lett. **28**, 816–818 (2003).

22. M. A. Choma, C. Yand, and J. A. Izatt, "Instantaneous quadrature low-coherence interferometry with 3×3 fiber optic couplers," Opt. Lett. **28**, 2162–2164 (2003).

23. R. J. Aldifi, W. J. MacIntyre, and R. Haaga, "The effects of biological motion in CT resolution," Am. J. Radiol. **127**, 11–15 (1976).

24. M. L. Wood and R. M. Henkelman, "NMR image artifact from periodic motion," Med. Phys. **12**, 143–151 (1985).

25. S. H. Yun, G. J. Tearney, J. F. de Boer, and B. E. Bouma, "Motion artifacts in optical coherence tomography with frequency-domain ranging," Opt. Express **12**, 2977–2998 (2004).

26. P. F. Moulton, "Spectroscopic and laser characteristics of $Ti:Al_2O_3$," J. Opt. Soc. Am. B **3**, 125–133 (1986).

27. A. M. Kowalevicz, T. Ko, I. Hart, and G. J. Fujimoto, "Ultrahigh resolution optical coherence tomography using a superluminescent light source," Opt. Express **10**, 349–353 (2002).

28. D. M. Gale, M. I. Pether, and J. C. Dainty, "Linnik microscope imaging of integrated circuit structures," Appl. Opt. **35**, 131–148 (1996).